

Periodic Lattice Porous Structure Produced by Selective Laser Melting: Process, Experiment and Numerical Simulation Analysis

Jianrui Zhang^{1,2}, Min Chi¹, Bo Qian^{1,*} and Zhijun Qiu²

¹School of Mechanical and Power Engineering, East China University of Science and Technology, Shanghai, 200237, China

²School of Mechanical, Materials, Mechatronic and Biomedical Engineering, University of Wollongong, Wollongong, Australia

*Corresponding Author: Bo Qian. Email: qianbo@ecust.edu.cn

Received: 08 March 2020; Accepted: 24 June 2020

Abstract: To accurately perform the coupled simulation of temperature field and stress field of complex parts and porous structures under the optimal manufacturing process parameters, three kinds of porous structures with different complexity were designed in this paper. Firstly, ANSYS additive software was used to conduct the stress/deformation simulation of the whole structure under different scanning strategies. Secondly, the optimal scanning strategy for different porous structures was determined, then the experimental preparation was performed, and mechanical properties of compression were tested and studied. The results show that the elastic modulus and yield strength increase with the increase of pole diameter/wall thickness. In addition, the quasi-static compression simulation of different structures was performed, and the compression performance was analyzed based on the experimental data. Finally, the stress concentration region of different structures was obtained.

Keywords: Selective laser melting; numerical simulation; stress field; lattice porous structure

1 Introduction

Selective laser melting (SLM) is an additive manufacturing technique in which metal powders are melted in layers and superimposed to form solid metal parts. After the post-processing, high density parts can be obtained [1]. In recent years, SLM technology has been widely used in engineering applications. This technology is not constrained by the shape of parts in the manufacturing process, and can realize the innovative design of arbitrary complex structure [2]. During the forming process, under the thermal action of high energy laser beam, the metal powder material in the forming area is thoroughly melted and welded into solid metal after cooling. Subsequently, three-dimensional solid parts are rapidly formed by the accumulation of the above process [3]. SLM technology is a kind of solid free forming technology. By laser scanning each layer of powder material, it can make any complex shape of metal parts layer



This work is licensed under a Creative Commons Attribution 4.0 International License, which permits unrestricted use, distribution, and reproduction in any medium, provided the original work is properly cited.

by layer. Besides, it also has unique advantages such as complete melting, high hardness, rapid cooling, narrow heat-affected zone, reducing cracking sensitivity. In a word, a variety of complex functional precision structures and lightweight products can be designed and prepared through SLM technology [4–6].

In SLM forming process, the temperature field and stress field change rapidly, and are affected by many factors. Therefore, change law is difficult to be captured by experimental methods, and many experimental phenomena lack theoretical basis [7]. At present, simulation software is used to simulate micro and macro temperature stress and flow field in most researches on SLM forming process [8,9]. Through the establishment of the mathematical model, different simulation methods can be employed to quickly and accurately solve variable values in the model. Different from the experimental research, numerical simulation can accurately predict the problems in the forming process, and find the corresponding solutions through theoretical calculation. In this way, the time and economic cost are reduced, and the efficiency is greatly improved [10].

The three-dimensional lattice structure, first proposed by Evans et al. [11] of Harvard University in 2000, has a similar structural form to space truss structure. Porous lattice structure is characterized by low density and remarkable mechanical properties, and widely applied in aerospace, medical, biological and other fields [12]. There are two main categories of porous structures: one is the disordered porous foam structure; the other is the ordered periodic porous structure. Lattice structure is one of the three-dimensional periodic porous structures. The performance of lattice structure mainly depends on the geometric parameters and material properties of internal crystal cell structure [13–15]. In addition, Gu et al. [16–18] studied the manufacturing process of SLM forming cantilever structure, and analyze the relationship between forming structure and laser forming process. Through the combination of numerical simulation and process experiment, process optimization and structure improvement are carried out to realize the difficult forming structure with high strength and high toughness. In this paper, three different kinds of porous lattice structures were established, and the process, experiment and simulation calculation of selective laser melting were carried out. In addition, the optimal scanning strategy of SLM for different structure sizes and the compression mechanical properties of the samples were obtained.

2 Experimental Equipment and Materials

2.1 Experimental Equipment

YIBO RP SLM80 desktop SLM printer was used in this experiment, as shown in Fig. 1. The main components include the scanning system, forming system, control system and gas protection system. A single-mode fiber laser with a wavelength of 1080 nm was used in this experiment, the minimum spot diameter of the laser beam was 50 μm , and the maximum scanning speed of the laser was 1000 mm/s. The maximum forming size of the working cylinder was 80 mm \times 80 mm \times 100 mm, and the thickness of metal powder spreading was 20–100 μm . During the forming process, the movement loading of the laser beam and operation of the powder spreading device were controlled by software. To prevent the oxidation of metal powder during the forming process, the forming space was set as a sealed cavity, and argon was introduced as the protective gas, and the oxygen content in the manufacturing process was kept below 0.05%. Tab. 1 shows the main manufacturing process parameters of the experimental equipment.

2.2 Experimental Materials

316L stainless steel has superior mechanical properties, including excellent corrosion resistance, oxidation resistance, high heat resistance and good weldability. In this experiment, 316L

stainless steel with the size of 80 mm × 80 mm × 20 mm was used, and aerosol method was employed to prepare 316L stainless steel powder. Tab. 2 shows its chemical composition.



Figure 1: Experimental equipment

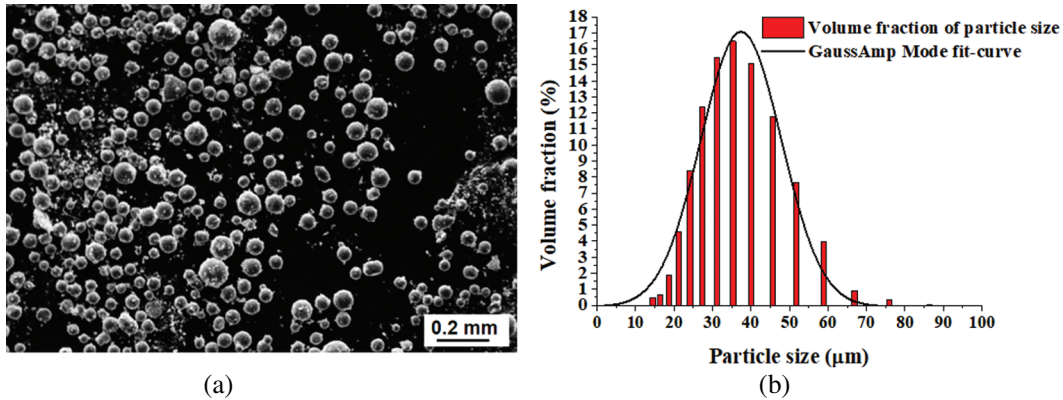
Table 1: Main parameters of SLM machine

| Name | Parameter |
|---|-----------|
| Maximum laser power (W) | 250 |
| Maximum scanning rate (mm/s) | 1000 |
| Laser spot diameter (μm) | 75 |
| Powder laying thickness (μm) | 35 |
| Forming (size/mm) | 80 × 80 |

In the SLM forming process, the high plasticity, good sphericity, fine powder size, good fluidity and high bulk density of metal powder materials are required [19]. Fig. 2a shows the micro morphology of the powder used in this experiment. Fig. 2b shows the particle size distribution of the powder. The particle size distribution of the powder was 15–67 μm , and the average particle size was 35 μm .

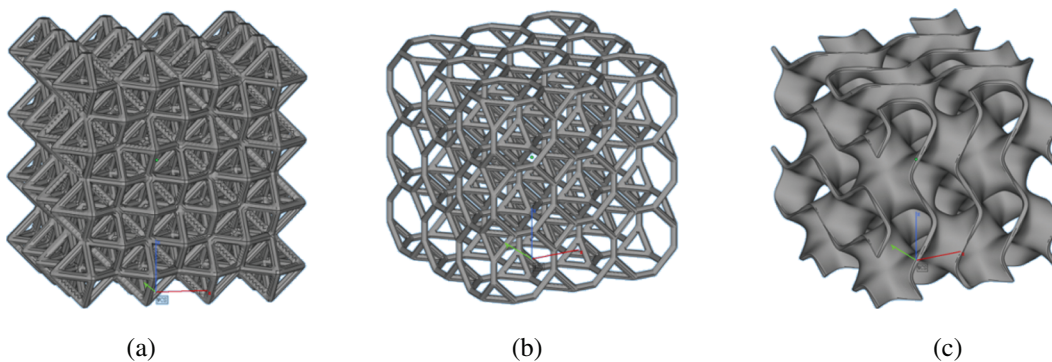
Table 2: Chemical composition of 316L stainless steel powder (wt,%)

| Fe | Cr | Ni | Mo | Mn | Si | P | O | S |
|------|-------|-------|------|------|-----|-----|--------|-------|
| Bal. | 16.79 | 10.66 | 2.42 | 2.42 | 0.2 | 1.0 | 0.0247 | 0.011 |

**Figure 2:** 316L stainless steel powder. (a) SEM micrograph and (b) Size distribution

3 Establishment and Numerical Simulation of Lattice Structure Model

3-Matic software and 3D Max software were used to establish octahedron, hexadecimal and gyroid lattice structure, as shown in Fig. 3. The octahedron lattice structure, as shown in Fig. 3a, is composed of four equilateral triangles and can be regarded as two regular vertebrae. Each regular vertebral body is composed of four triangles and a square. The regular octahedron lattice has six vertices, which are located in the centroid of the cube. Hexadecimal lattice structure, as shown in Fig. 3b, is composed of six regular octahedron lattices, and it can also be seen as a cube cutting four sharp angles through eight planes.

**Figure 3:** Establishment of lattice structure model. (a) Octahedron lattice structure, (b) Hexadecimal lattice structure, and (c) Gyroid

G-surface structure, as shown in Fig. 3c, was selected as the compression sample model with the complex surface. As a branch of average curvature surface, G-surface is a kind of

mathematical surface with 3-D periodicity, zero average curvature and large surface area (average curvature is defined as follows: there must be a maximum curvature and minimum curvature on any surface at a certain location in space, and the average curvature is the average of the maximum and minimum). G-surface divides the space into two interwoven subdomains while keeping the cavity open. The mathematical implicit function relation of a minimal surface is described as follows:

$$\Phi_G(x, y, z) = \cos(\omega x) \sin(\omega y) + \cos(\omega y) \sin(\omega z) + \cos(\omega z) \sin(\omega x) = c \quad (1)$$

where c is a constant which controls the shape of the surface and the surface area of the structure. If $c=0$, it is the G surface. ω is a coefficient, which indicates the number of periodicity. In other words, if $\omega=2\pi$, there is a minimal surface element in a $1 \times 1 \times 1$ cube with a period.

In this paper, 3D Max software was used to draw G-surface model, and the drawing process was shown in Fig. 4. Firstly, a hexagonal surface was drawn, as shown in Fig. 4a. Secondly, the drawn hexagonal surface was mirrored, copied, rotated and spliced to complete a unit surface piece, as shown in Fig. 4b. Thirdly, the surface of the unit surface piece was smoothed, and the corresponding wall thickness was given to form a G-surface element body, as shown in Fig. 4c. After the completion of Gyroid minimal surface element body, the element body was arrayed to obtain the compressed sample model, as shown in Fig. 4d. The design parameters of each porous structure model are shown in Tab. 3.

To predict the residual stress and deformation after SLM forming, ANSYS additive module was used to simulate the residual stress of two kinds of porous lattice structure models. Gu et al. [19,20] has finished a lot of pioneering work in this respect. The thermal strain simulation provides a high degree of accuracy by predicting how the thermal cycle affects the strain accumulation at each location within a part [21]. In this algorithm, the intrinsic strain was used, and the local correction of the intrinsic strain was realized by the thermal ratchet effect. At the same time, J2 plastic stress mode was used to realize the elastic-plastic behavior of materials.

Since the scanning mode also has a crucial influence on the quality of SLM formed parts, numerical simulation of residual stress distribution under different scanning parameters was carried out. Qian et al. [22,23] found that proper scanning strategies can reduce manufacturing residual stress and the generation of warpage, and improve the accuracy and surface quality of parts. For the three different complex porous structures to be studied in this chapter, the optimal scanning strategy of each structure was determined by simulating the forming residual stress under different scanning strategies.

Fig. 5 shows the residual stress distribution of octahedral porous model under different scanning strategies. As shown in Fig. 5, the maximum residual stress of the formed part under X-ray scanning is 1.144×10^9 Pa, the maximum residual stress of 45° scanning is 1.157×10^9 Pa, the maximum residual force of 67° scanning is 1.201×10^9 Pa, and the maximum residual stress of XY scanning is 1.143×10^9 Pa. Therefore, the best scanning strategy for the octahedron lattice structure is 45° scanning.

Fig. 6 shows the residual stress distribution of the hexadecimal lattice model under different scanning strategies. As shown in Fig. 6, the maximum residual stress of the formed part under X-direction scanning is 1.294×10^9 Pa, the maximum residual stress of 45° scanning is 1.217×10^9 Pa, the maximum residual force of 67° scanning is 1.433×10^9 Pa, and the maximum residual stress of XY scanning is 1.199×10^9 Pa. It can be seen that the best scanning strategy for the hexadecimal lattice structure is XY scanning.

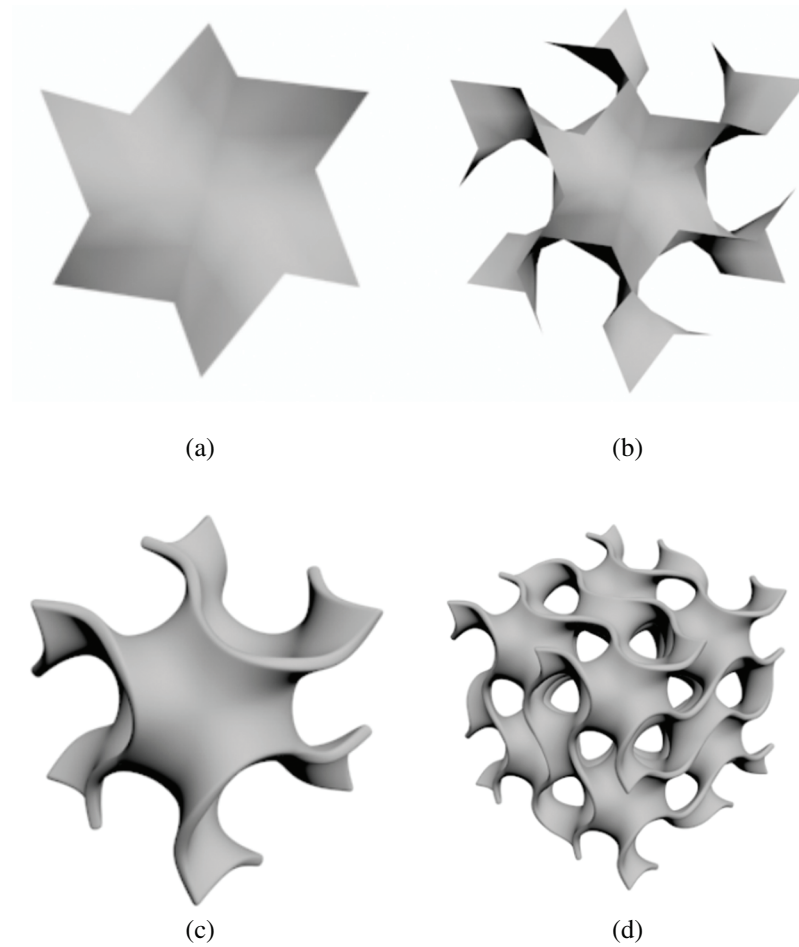


Figure 4: The model of compression sample

Table 3: Design parameters of porous structure model

| Model | Model size | Pole diameter/wall thickness |
|-------------------------------|-----------------------|------------------------------|
| Octahedron lattice structure | 15 mm × 15 mm × 15 mm | 0.4 mm/0.8 mm/1.2 mm |
| Hexadecimal lattice structure | 15 mm × 15 mm × 15 mm | 0.4 mm/0.8 mm/1.2 mm |
| Gyroid structure | 15 mm × 15 mm × 15 mm | 0.5 mm/0.65 mm/0.8 mm |

Fig. 7 shows the residual stress distribution of the gyroid structure under different scanning strategies. It can be seen from the figure that the maximum residual stress of the formed part under X-direction scanning is 1.208×10^9 Pa, the maximum residual stress of 45° scanning is 1.231×10^9 Pa, the maximum residual force of 67° scanning is 1.242×10^9 Pa, and the maximum residual stress of XY scanning is 1.229×10^9 Pa. Therefore, the best scanning strategy for the structure of the gyroid body is X-direction scanning.

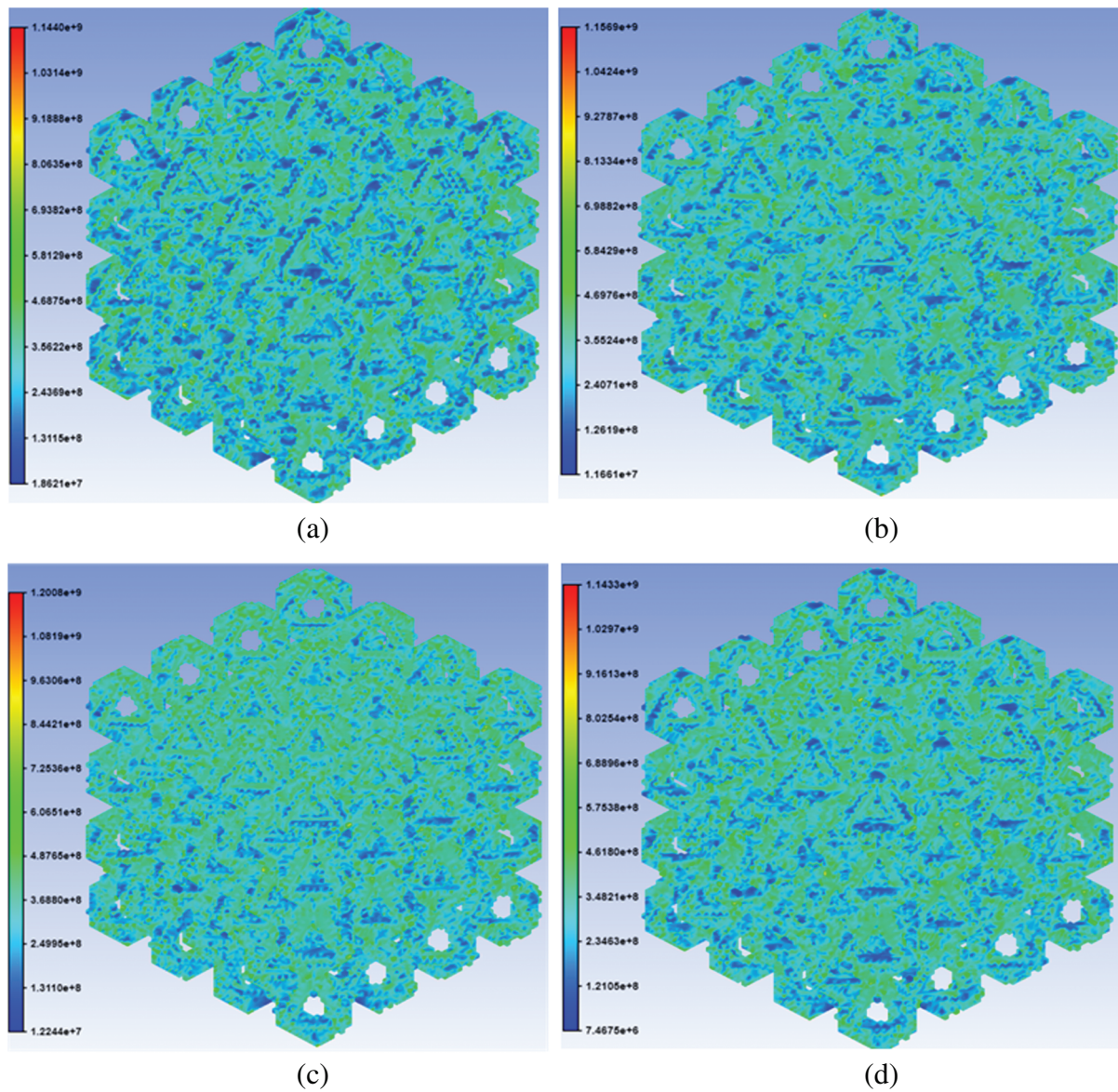


Figure 5: Residual stress distribution of octahedron lattice structure under different scanning strategies. (a) X direction scanning, (b) 45° scanning, (c) 67° scanning and (d) XY scanning

4 Preparation and Result Analysis of Three Lattice Porous Structures

4.1 Sample Preparations

As shown in Fig. 8, three kinds of SLM forming experiments with periodic and complex structure were carried out by YIBO RP SLM80 desktop SLM printer. 316L stainless steel powder was used as the experimental material. Three structures were prepared and obtained by 45° , XY and X-direction scanning. The quasi-static compression tests were carried out on three samples with different diameters/wall thicknesses of periodic and complex structures by a universal testing machine. The loading speed set in the test was 1 mm/min.

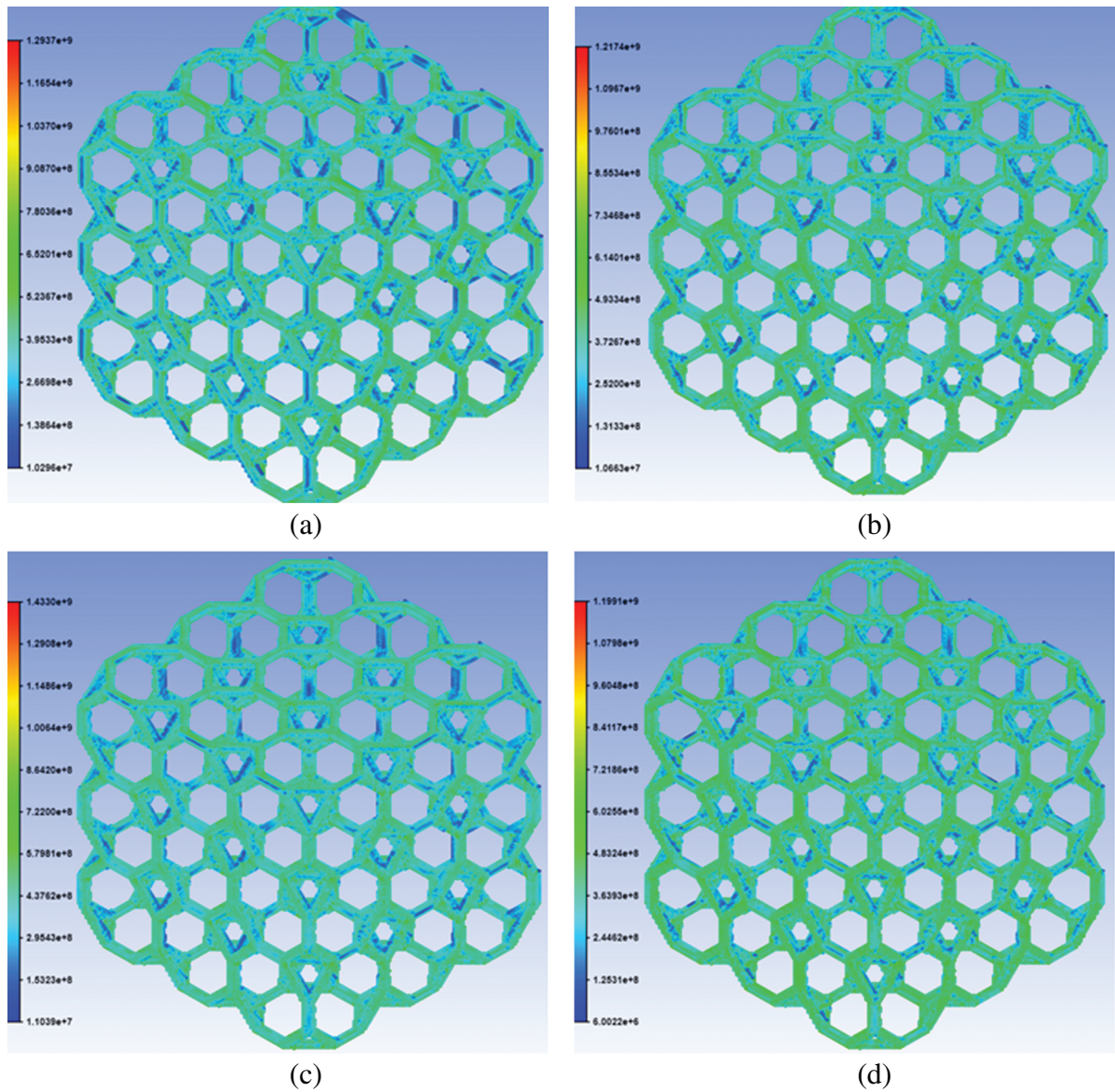


Figure 6: Residual stress distribution of the hexadecimal lattice structure under different scanning strategies. (a) X direction scanning, (b) 45° scanning, (c) 67° scanning and (d) XY scanning

4.2 Morphology Analysis

Fig. 9 shows the electron micrograph of octahedron lattice structure with different pole diameters. Since the octahedron round pole structure has a certain inclination angle with the horizontal plane, the edge liquid metal tends to seep into the metal powder particles in the SLM layered forming process, and the surrounding powder is adhered to the forming entity during the solidification, as shown in Fig. 9d. Due to the large number of particles and spheroidization, the surface of the pole structure is rough.

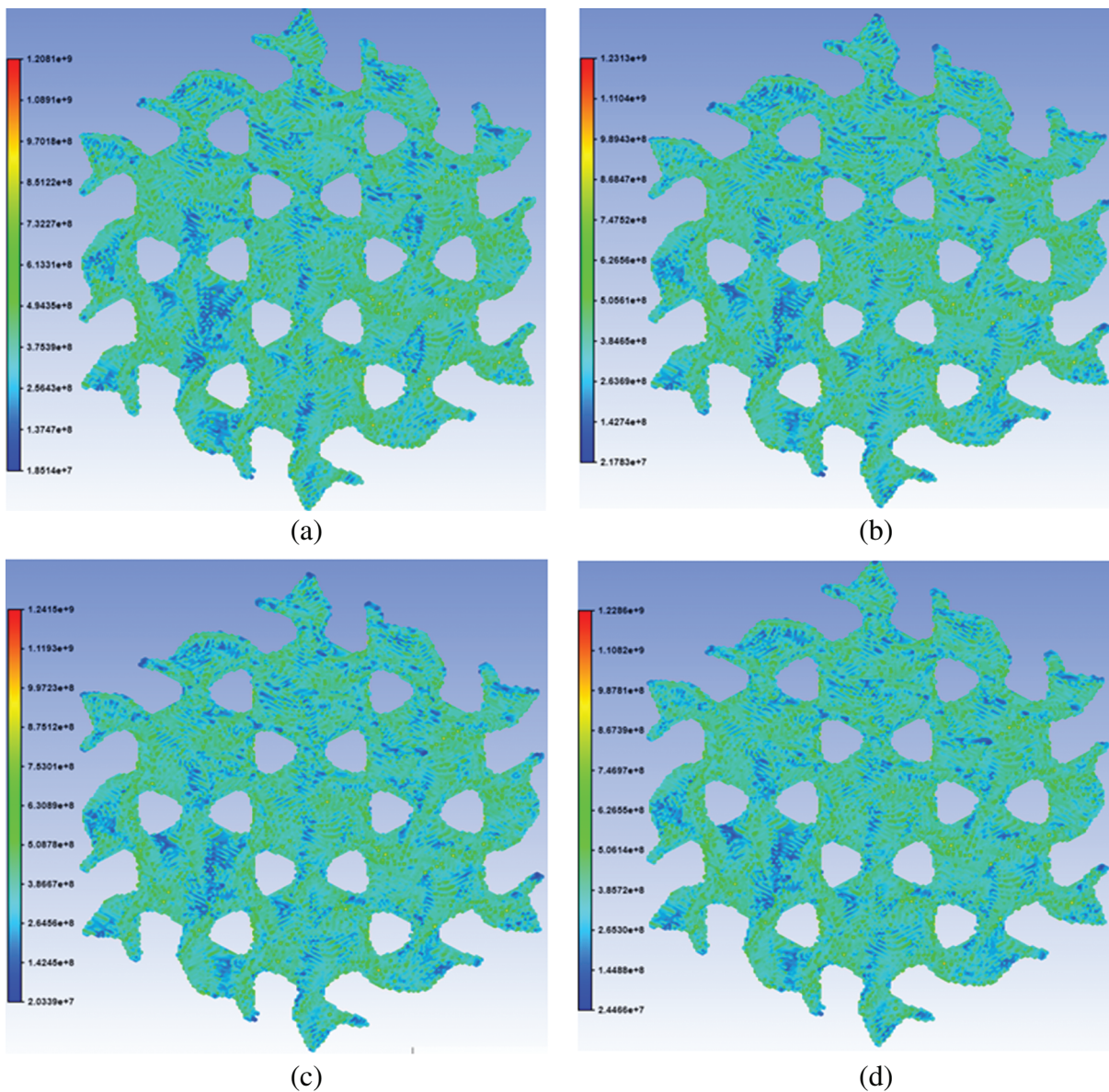


Figure 7: Residual stress distribution of gyroid structure under different scanning strategies. (a) X direction scanning, (b) 45° scanning, (c) 67° scanning and (d) XY scanning

Fig. 10 is an electron micrograph of a hexadecimal lattice sample with different pole diameters. As shown in Fig. 10d, a clear scanning path can be observed on the upper surface, while there is the rough edge of the pole structure, spheroidization and more attached powder particles.

5 Compression Experiment and Result Analysis of Porous Lattice Structures

5.1 Experiment on Octahedron Lattice Structure and Result Analysis

Fig. 11 shows engineering stress-strain curves of the octahedron lattice structure under the quasi-static compression, and the sample is subject to the axial deformation during the

compression. As shown in Fig. 11, each curve is composed of elastic stage, compression stage and compaction stage.

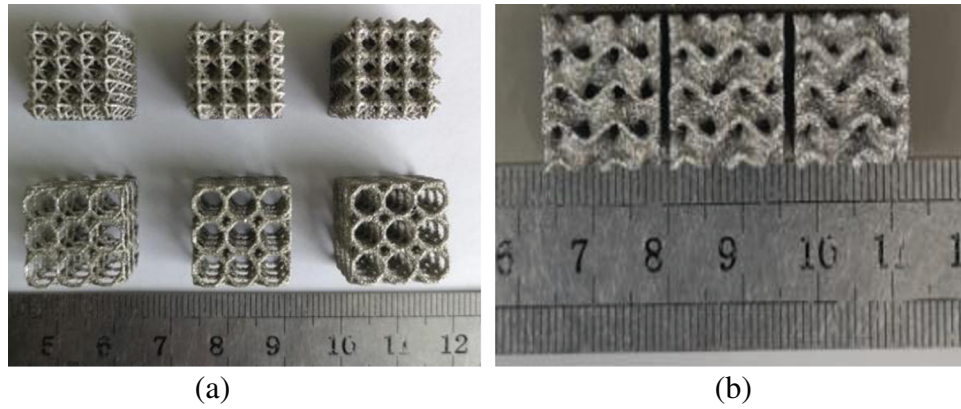


Figure 8: Kinds of SLM forming experiments. (a) Samples with porous structure and (b) gyroid sample

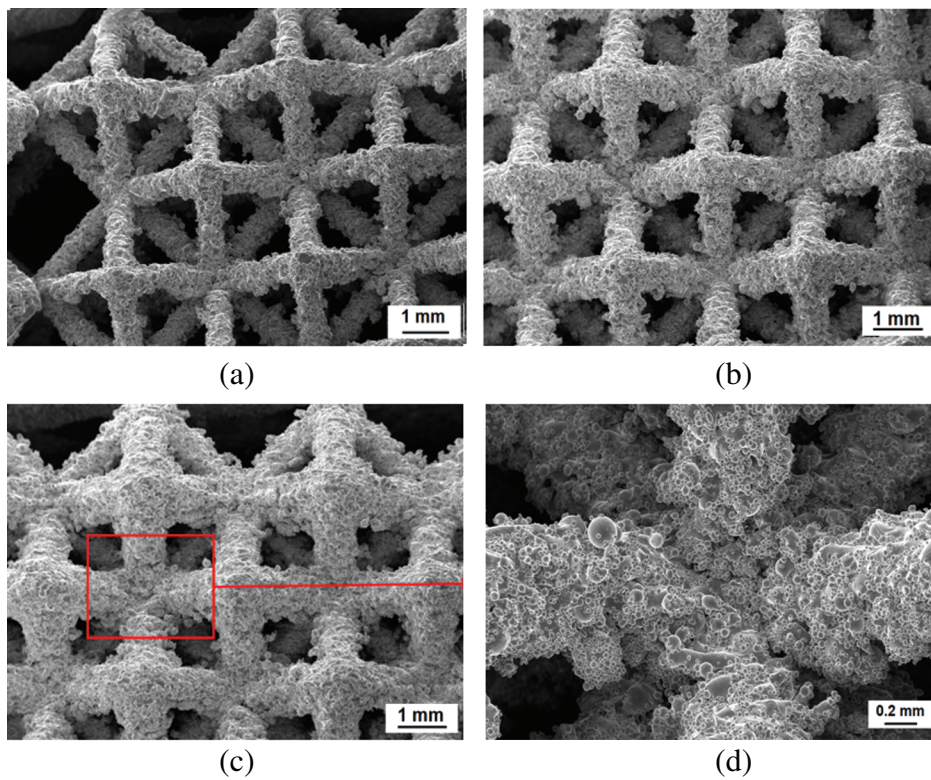


Figure 9: SEM morphology of octahedron lattice structure. (a) $d = 0.5$ mm, (b) $d = 0.65$ mm, (c) $d = 0.8$ mm and (d) $d = 0.8$ mm

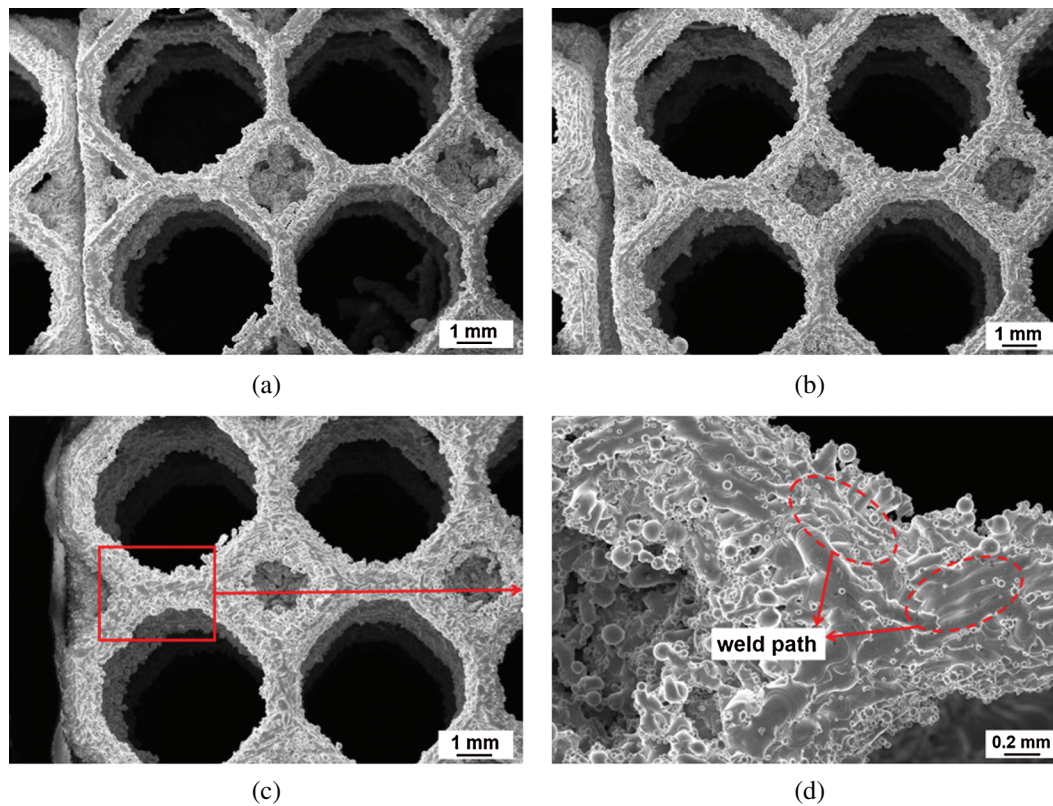


Figure 10: SEM morphology of hexadecimal porous structure. (a) $d = 0.5$ mm, (b) $d = 0.65$ mm, (c) $d = 0.8$ mm and (d) weld path

In the elastic stage, elastic deformation mainly occurs; the compression stress and displacement increase rapidly and linearly. The slope of this curve is the elastic modulus. As shown in Fig. 11, the elastic modulus of octahedron lattice structure increases with the increase of the pole diameter.

In the compression stage, plastic deformation mainly occurs. With the increase of compression displacement, the compression stress changes slightly. For some structures with small strength, the fluctuation of compression stress is also accompanied by the structural failure of sample in this stage. As shown in Fig. 11b, when the pole diameter of lattice structure is small ($d = 0.5$ mm), there are several obvious fluctuations on the curve in the compression stage. It indicates that the structure in the sample is broken during the compression. With the increase of the diameter of lattice pole, the fluctuation of the compression stage in the curve decreases and tends to be smooth, and the yield point increases gradually. It indicates that the compressive performance of the sample is enhanced (as shown in Figs. 11c and 11d), while the duration of the compression stage decreases.

In the compaction stage, with the increase of compression displacement, the compression stress increases continuously until the sample is completely compacted. The compressive stress increases with the increase of pole diameter of the sample.

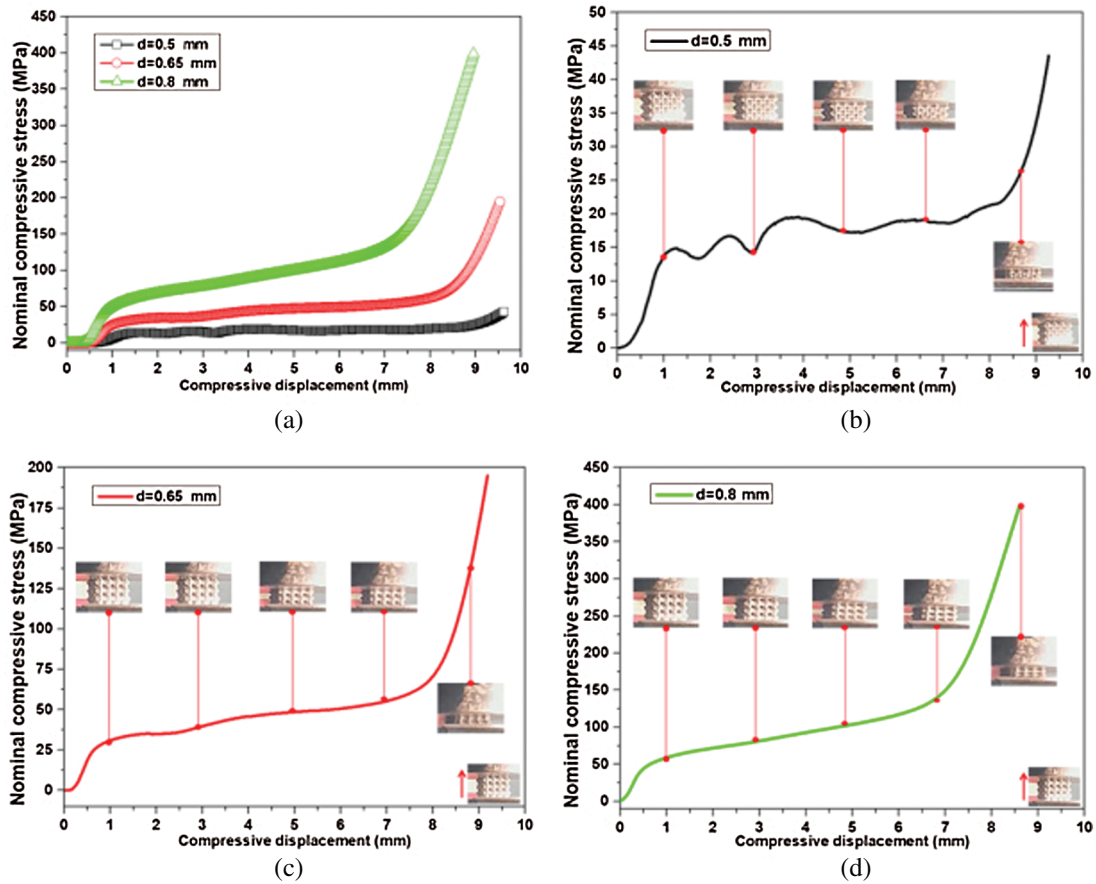


Figure 11: Compression engineering stress-strain curve of octahedron lattice structure sample. (a) Comparison chart, (b) $d = 0.5$ mm, (c) $d = 0.65$ mm and (d) $d = 0.8$ mm

5.2 Analysis of Experimental Results of the Hexahedron Porous Structure Sample

Fig. 12 shows the engineering stress-strain curve of the hexadecimal lattice structure under the quasi-static compression, and the sample is subject to axial deformation during the compression process. As shown in Fig. 12a, in the elastic stage, elastic modulus increases with the increase of the pole diameter of the octahedron lattice structure; in the compression stage, as shown in Fig. 12b, when the diameter of the lattice pole structure is small ($d = 0.5$ mm), the curve fluctuates greatly in the compression stage. It indicates that the structure of the sample has been broken for many times during the compression. With the increase of the lattice pole diameter, the fluctuation of the compression stage of the curve decreases, and the yield point increases gradually. It indicates that the compressive performance of the sample is enhanced (as shown in Figs. 12c and 12d).

5.3 Analysis of Experimental Results of the Gyroid Structure

Fig. 13 displays the engineering stress-strain curve of the gyroid structure under the compression, and the sample is subject to axial deformation during the compression. It can be seen from the figure that in the elastic stage, when the wall thickness is 0.4 mm, the elastic modulus is 1.44 GPa; and when the wall thickness increases to 0.8 mm and 1.2 mm, the elastic modulus

is 2.60 GPa and 3.21 GPa, respectively. With the increase of the wall thickness of gyroid, the elastic modulus increases. In the compression stage, with the increase of compression displacement, the change of compression stress is the smallest when the wall thickness is $h = 0.4$ mm; and with the increase of the wall thickness, the yield strength of the sample increases gradually. In the compaction stage, with the increase of compression displacement, the compression stress increases continuously until the sample is fully compacted. The compressive stress of the sample increases with the increase of the pole diameter of the sample.

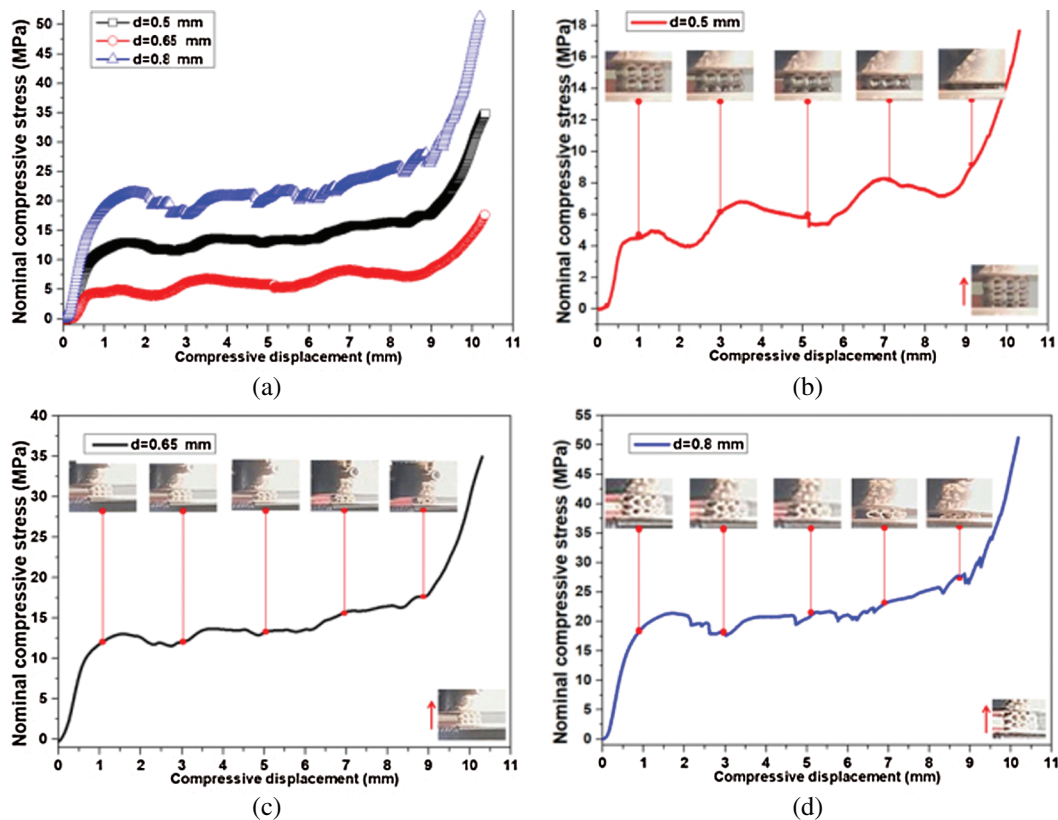


Figure 12: Compression engineering stress-strain curve of hexadecagonal lattice structure specimen. (a) Comparison chart, (b) $d = 0.5$ mm, (c) $d = 0.65$ mm and (d) $d = 0.8$ mm

6 Simulation Analysis of Porous Lattice Structure Compression

6.1 Compression Models of Porous Lattice Structure

STL triangular patch models of three porous structures established in Chapter 2 were introduced into SCDM pre-processing software for substantiation, and three complex structures models with the minimum pole diameter/wall thickness were simulated by ANSYS Workbench finite element simulation software for the quasi-static compression. As shown in Fig. 14, the axial compression finite element model of three structures was established. To reduce the calculation amount, octahedron lattice structure was simplified to 1/4 model (as shown in Fig. 14a). Hexahedral mesh of 20 nodal points of SOLID186 was used for the model meshing. A vertical downward displacement load was set on the top plate, and the rigid plate and the structure were

defined as the side-side binding contact. The hard contact algorithm was adopted in the normal behavior, and the tangential friction coefficient was ignored. The contact between the three porous structure models and rigid surface is frictionless hard contact. The lower rigid surface keeps still, and the upper rigid surface is shifted negatively along the Y axis by 10 mm. In order to ensure that there is no significant impact on the model during loading, the displacement loading follows the smooth loading mode (Smooth Step), and the analysis time is set to 0.001 s.

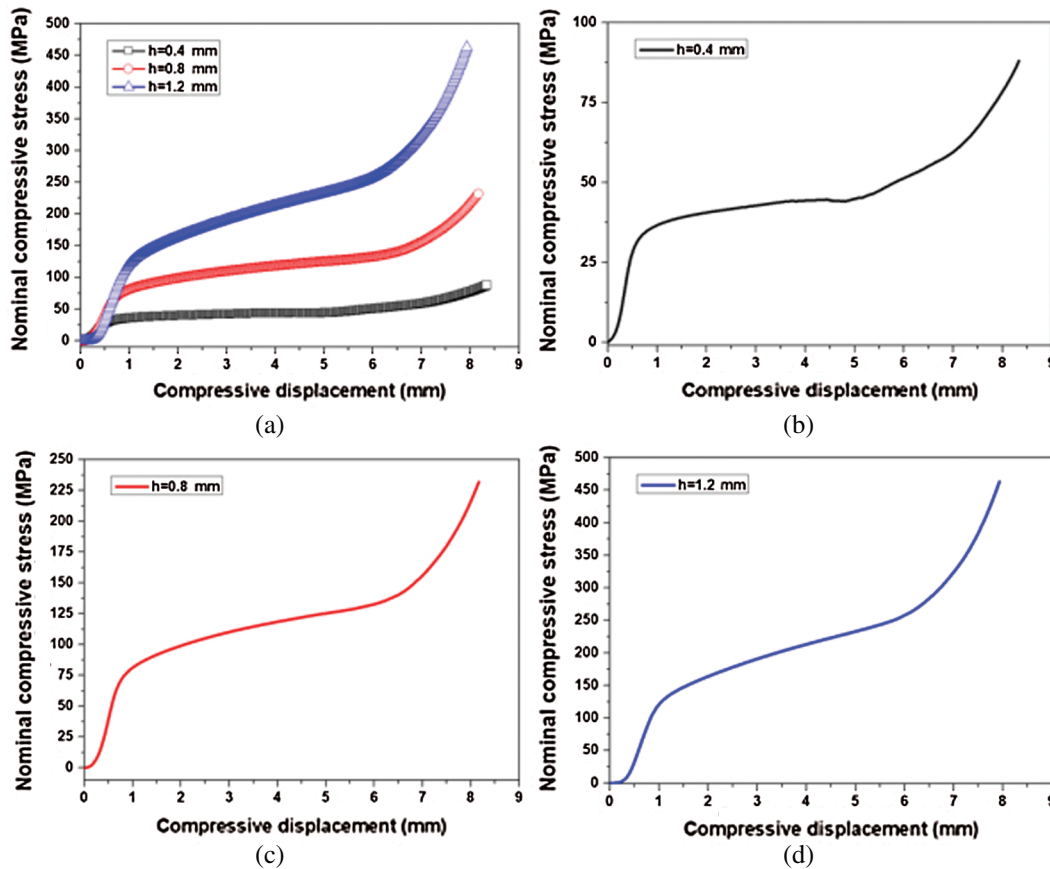


Figure 13: Compression engineering stress-strain curve of gyroid specimen. (a) Comparison chart, (b) $d = 0.4$ mm, (c) $d = 0.8$ mm and (d) $d = 1.2$ mm

6.2 Analysis of Compression Simulation Results

As shown in Fig. 15, simulation results of axial quasi-static compression of octahedron lattice structure are presented. Since the contact area between the upper and lower plane of octahedron lattice structure and the compression plate is small, the stress is mainly concentrated in the connecting area of the round pole at the upper and lower ends, and the stress in the middle area is small. As shown in Fig. 15b, during the compression process, both the experimental test and simulation results show the compression stage after the yield point. Due to the stress concentration in the experimental sample and the fracture failure of some members, the compression stage fluctuates; while the ideal elastic-plastic material is used in the finite element simulation,

in which the fracture failure of the material is ignored. Therefore, a smooth compression stage is maintained.

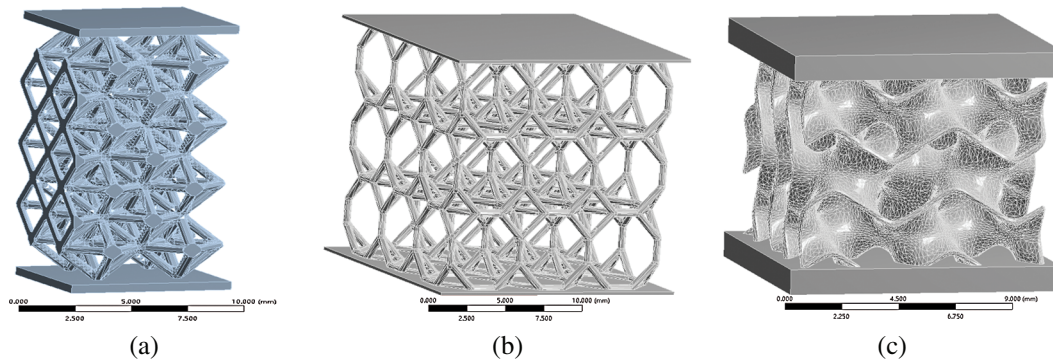


Figure 14: The FEA model. (a) Octahedron lattice structure, (b) Hexadecimal porous structure and (c) gyroid

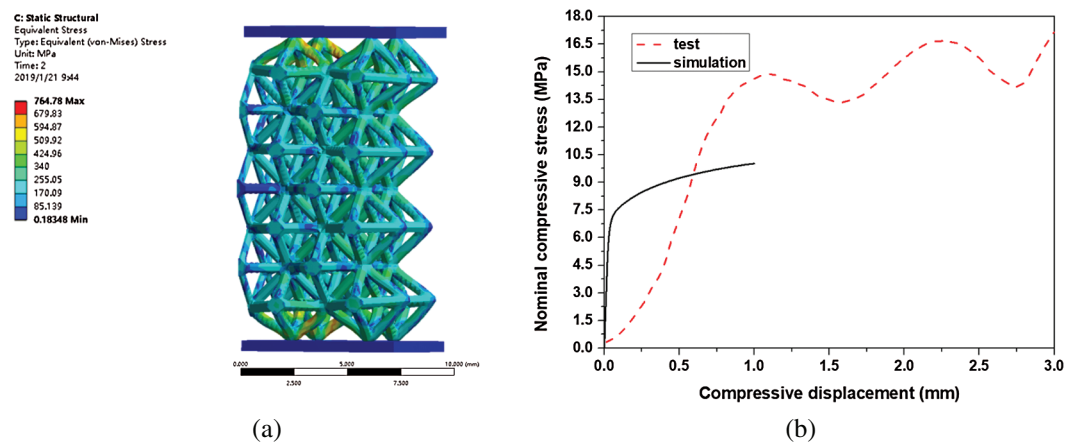


Figure 15: Quasi-static analytical result of octahedron lattice structures. (a) Mises distribution and (b) Compress stress-strain curves

As shown in Fig. 16, the simulation results of the quasi-static compression of the hexadecimal lattice structure are presented. It can be seen the maximum stress of the hexadecimal porous structure is concentrated in the internal vertical pole region, and the stress in other regions is smaller. As shown in Fig. 16b, during the compression process, both the experimental test and simulation results show the compression stage after the yield point. The vertical member with more concentrated stress in the sample is fractured, the compression stage fluctuates. However, the ideal elastic-plastic material is used in the finite element simulation in which the fracture failure of the material is not considered. Therefore, a smooth compression stage is maintained.

As shown in Fig. 17, simulation results of the axial quasi-static compression of the gyroid structure are presented. It can be seen that the maximum stress of the gyroid structure is distributed in the area with the minimum curvature of the surface, and the stress at the edge

of the surface is small. The strength of the gyroid structure is higher, and the internal structure is less damaged in the actual compression process. Therefore, the trend of the experimental test and simulation results curve is consistent in the elastic stage and the compression stage (as shown in Fig. 17b).

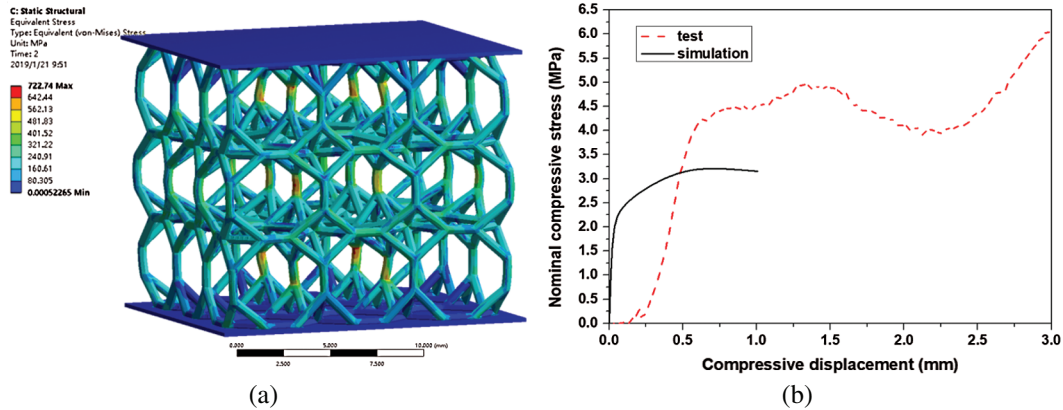


Figure 16: Quasi-static analytical result of hexadecimal lattice structures. (a) Mises distribution and (b) Compress stress-strain curves

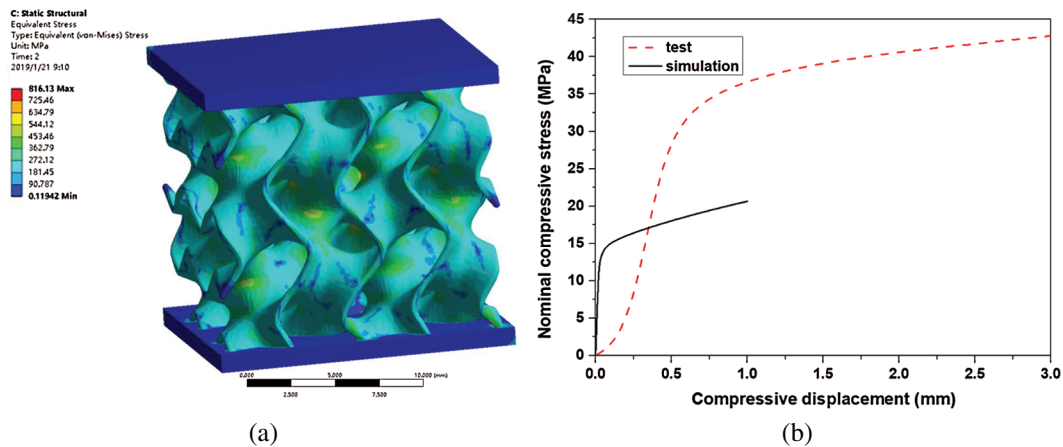


Figure 17: Quasi-static analytical result of gyroid structures. (a) Mises distribution and (b) Compress stress-strain curves

6.3 Comparative Analysis of Compression Simulation and Compression Test

The elastic modulus of quasi-static compression simulation of three complex porous structures is larger than that of compression experiment, while the yield strength of the former is smaller than that of the latter. This is mainly caused layered manufacturing in the SLM forming process. Due to the spheroidization and the attached powder particles on the surface of the parts during the forming process, there is a certain size and accuracy deviation between the final formed experimental sample and the theoretical model. In addition, some factors are ignored in

the simulation calculation, such as the material embrittlement fracture, leading to a certain error between the simulation and the experimental results.

7 Conclusion

In this paper, compression mechanical properties of the three periodic porous structures are analyzed. The main conclusions are as follows:

- (1) For three different structures, the residual stress is simulated under different scanning strategies to obtain the optimal scanning parameters. Forming experiments under the optimized parameters are carried out, and the compression stress deformation curves under different pole diameters/wall thicknesses are obtained.
- (2) The quasi-static compression simulation of different structures is carried out, and the compression performance is analyzed with the experimental data. The experimental results show that the compression of periodic porous structure can be divided into three stages: elastic stage, compression stage and compaction stage.
- (3) In the compression process, the maximum Mises stress distribution of octahedron lattice structure is concentrated in the connection region of the round poles at the upper and lower ends; that of the hexadecimal lattice structure is concentrated in the internal vertical pole region; and that of the gyroid structure is concentrated in the minimum curvature region of the curved surface.

Funding Statement: This paper was funded by the Key Project of Chinese National Programs for Fundamental Research and Development—Model Processing and Process Planning Software Project for Additive Manufacturing (2018YFB1105300)—Universal Full-dimension Digital Model Project (2018YFB1105301).

Conflicts of Interest: The authors declare that they have no conflicts of interest to report regarding the present study.

References

1. Jerrard, P. G. E., Hao, L., Evans, K. E. (2009). Experimental investigation into selective laser melting of austenitic and martensitic stainless steel powder mixtures. *Proceedings of the Institution of Mechanical Engineers*, 223(11), 1409–1416.
2. Shahir, M. Y., Chen, Y. F., Richard, B., Yang, S. F., Gao, N. (2017). Investigation on porosity and microhardness of 316L stainless steel fabricated by selective laser melting. *Metals*, 7(64), 1–12.
3. Amato, K. N., Gaytan, S. M., Murr, L. E., Martinezab, E., Shindoab, P. W. et al. (2012). Microstructures and mechanical behavior of Inconel 718 fabricated by selective laser melting. *Acta Materialia*, 60(5), 2229–2239.
4. Ghosh, S. K., Bandyopadhyay, K., Saha, P. (2014). Development of an in-situ multi-component reinforced Al-based metal matrix composite by direct metal laser sintering technique—optimization of process parameters. *Materials Characterization*, 93, 68–78. DOI 10.1016/j.matchar.2014.03.021.
5. Attar, H., Bnisch, M., Calin, M., Zhang, L. C., Scudino, S. et al. (2014). Selective laser melting of in situ titanium-titanium boride composites: processing, microstructure and mechanical properties. *Acta Materialia*, 76, 13–22. DOI 10.1016/j.actamat.2014.05.022.
6. Louvis, E., Fox, P., Sutcliffe, C. J. (2011). Selective laser melting of aluminium components. *Journal of Materials Processing Technology*, 211(2), 275–284. DOI 10.1016/j.jmatprotec.2010.09.019.
7. Roberts, I. A., Wang, C. J., Esterlein, R., Stanford, M., Mynors, D. J. (2009). A three-dimensional finite element analysis of the temperature field during laser melting of metal powders in additive

- layer manufacturing. *International Journal of Machine Tools & Manufacture*, 49(12), 916–923. DOI 10.1016/j.ijmachtools.2009.07.004.
8. Dai, K., Shaw, L. (2004). Thermal and mechanical finite element modeling of laser forming from metal and ceramic powders. *Acta Materialia*, 52(1), 69–80.
 9. Dai, K., Shaw, L. (2001). Thermal and stress modeling of multi-material laser processing. *Acta Materialia*, 49(20), 4171–4181.
 10. Hussein, A., Hao, L., Yan, C., Eversonet, R. (2013). Finite element simulation of the temperature and stress fields in single layers built without-support in selective laser melting. *Materials & Design*, 52(24), 638–647.
 11. Evans, A. G., Hutchinson, J. W., Fleck, N. A., Ashby, M. F., Wadley, H. N. G. (2001). The topological design of multifunctional cellular metals. *Progress in Materials Science*, 46(3–4), 309–327.
 12. Chen, S. Y., Huang, J. C., Pan, C. T., Lin, C. H., Yang, T. L. et al. (2017). Microstructure and mechanical properties of open-cell porous Ti-6Al-4V fabricated by selective laser melting. *Journal of Alloys and Compounds*, 713, 248–254. DOI 10.1016/j.jallcom.2017.04.190.
 13. Wong, K. K., Leong, K. C. (2018). Saturated pool boiling enhancement using porous lattice structures produced by selective laser melting. *International Journal of Heat & Mass Transfer*, 121, 46–63. DOI 10.1016/j.ijheatmasstransfer.2017.12.148.
 14. Wang, D., Yang, Y., Liu, R., Xiao, D., Sun, J. F. (2013). Study on the designing rules and processability of porous structure based on selective laser melting (SLM). *Journal of Materials Processing Technology*, 213(10), 1734–1742.
 15. Choy, S. Y., Sun, C. N., Leong, K. F., Wei, J. (2017). Compressive properties of functionally graded lattice structures manufactured by selective laser melting. *Materials & Design*, 131, 112–120. DOI 10.1016/j.matdes.2017.06.006.
 16. Chen, H. Y., Gu, D. D., Xiong, J. P., Xia, M. (2017). Improving additive manufacturing processability of hard-to-process overhanging structure by selective laser melting. *Journal of Materials Processing Technology*, 250, 99–108. DOI 10.1016/j.jmatprotec.2017.06.044.
 17. Guo, B. S., Song, M., Yi, J. H., Ni, S. (2017). Improving additive manufacturing processability of hard-to-process overhanging structure by selective laser melting. *Materials Science & Engineering A*, 120, 307–316.
 18. Gu, D. D., Chen, Y. H. (2018). Selective laser melting of high strength and toughness stainless steel parts: the roles of laser hatch style and part placement strategy. *Materials Science & Engineering A*, 725, 419–427. DOI 10.1016/j.msea.2018.04.046.
 19. Gu, D. D., He, B. (2016). Finite element simulation and experimental investigation of residual stresses in selective laser melted Ti-Ni shape memory alloy. *Computational Materials Science*, 117(6), 221–232. DOI 10.1016/j.commatsci.2016.01.044.
 20. Shi, Q., Gu, D. D., Xia, M., Cao, S., Rong, T. (2016). Effects of laser processing parameters on thermal behavior and melting/solidification mechanism during selective laser melting of TiC/Inconel 718 composites. *Optics & Laser Technology*, 84, 9–22. DOI 10.1016/j.optlastec.2016.04.009.
 21. Li, Y., Zhou, K., Shu, B. T., Chua, C. K., Leong, K. F. (2017). Heat transfer and phase transition in the selective laser melting process. *International Journal of Heat & Mass Transfer*, 108, 2408–2416. DOI 10.1016/j.ijheatmasstransfer.2017.01.093.
 22. Qian, B., Shi, Y. S., Wei, Q. S., Wang, H. B. (2012). The helix scan strategy applied to the selective laser melting. *International Journal of Advanced Manufacturing Technology*, 63(5–8), 631–640. DOI 10.1007/s00170-012-3922-9.
 23. Li, B., Qian, B., Xu, Y., Liu, Z. Y., Xuan, F. Z. (2019). Fine-structured CoCrFeNiMn high-entropy alloy matrix composite with 12 wt% TiN particle reinforcements via selective laser melting assisted additive manufacturing. *Materials Letters*, 252, 88–91.